Supporting information

Correlated X-ray Ptychography and Fluorescence Nano-Tomography on the Fragmentation Behavior of an Individual Catalyst Particle During the Early Stages of Olefin Polymerization

Koen W. Bossers[†], Roozbeh Valadian[†], Silvia Zanoni[†], Remy Smeets[‡], Nic Friederichs[‡], Jan Garrevoet[ŧ], Florian Meirer[†], Bert M. Weckhuysen*[,†]

[†] Inorganic Chemistry & Catalysis, Debye Institute for Nanomaterials Science, Utrecht University, 3584 CG Utrecht, The Netherlands
[‡] SABIC, P.O. Box 319, 6160 AH Geleen, Netherlands
[ŧ] Photon Science at Deutsches Elektronen-Synchrotron DESY, Hamburg, 22603, Germany
*** Corresponding Author:** Bert Weckhuysen (b.m.weckhuysen@uu.nl)

Experimental section

1. Limiting Modes of Fragmentation

Two limiting modes for the fragmentation behavior of polyolefin catalysts have been observed experimentally and are schematically drawn in Figure S1. These two limiting modes are respectively, the so-called 'shrinking core' or 'layer-by-layer' fragmentation where the fragmentation of the catalyst particle starts at the outer surface of the particle by peeling-off framework species until finally the core is reached. The second mode is called the 'continuous bisection' mode where the catalyst particle instantaneously breaks up into successively smaller fragments due to the stress induced by the formed polymer inside the core of the particle. Depending on catalyst properties and reaction conditions such as friability of the catalyst particle matrix, pore size and pore size distribution and addition of co-monomers before or during the polymerization reaction one of these two limiting modes of fragmentation can be dominating.[1-7]

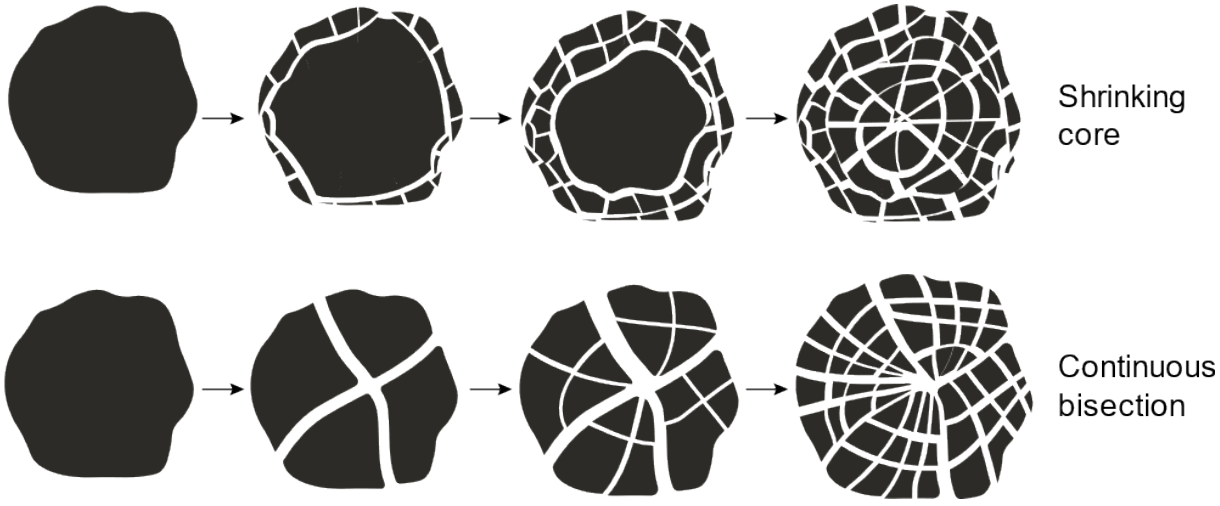

Figure S1. Schematic representation of the two limiting modes of fragmentation of the catalyst support matrix: shrinking core or layer-by-layer and continuous bisection. Adapted from[1].

2. Synthesis of the Ziegler-Natta Catalyst

A fourth generation Ziegler-Natta catalyst, representative for industrial propylene polymerization was prepared analogous to the procedure as described in patent EP2027164[8]. The material made has a final catalyst formulation of $MgCl_2/TiCl_4$/Dibutyl phthalate with a Ti weight loading of 2%, as measured with Inductively Coupled Plasma- Atom Emission Spectroscopy (ICP-AES). Analysis of the average particle size (D_{50}), using Static Laser Scattering (SLS) and measured with a Mastersizer 3000 laser diffraction particle size analyzer instrument, showed a D_{50} of 18 µm. Scanning Electron Microscopy (SEM) images, taken with a Phenom Pro at 15 kV accelerating voltage, of the pristine Ziegler-Natta catalyst are shown in Figure S2. The final catalyst has a surface area (S_{BET}) of 355 m^2/g, and pore volume (V_{pore}) of 0.279 cm^3/g with a pore size distribution mainly between 2-10 nm as determined with N_2 physisorption. The large cracks observed throughout the pristine catalyst particle, which are almost reminiscent of a smiley-face, are introduced unintentionally during the final drying step of the catalyst material.

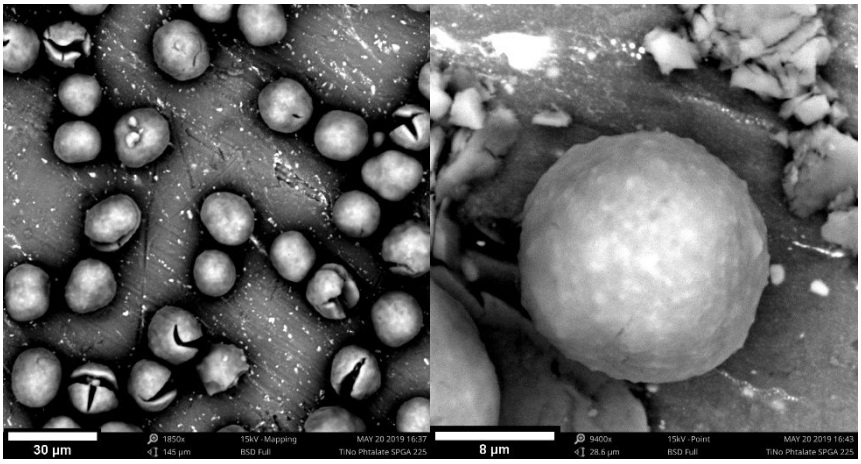

Figure S2 Scanning Electron Microscopy (SEM) images of the pristine Ziegler-Natta catalyst particles under study. A portion of the pristine catalyst particles show large cracks in the absence of α-olefin polymerization and is introduced during the final drying step of the catalyst material. SEM images were taken with a Phenom Pro SEM instrument using an accelerating voltage of 15 kV inside a N_2 filled glovebox operating at <1 ppm of H_2O and O_2.

3. Slurry-phase Propylene Polymerization

All catalyst handling and polymerization reactions were performed under inert conditions of nitrogen at room temperature. In a dried 500 mL three-necked round-bottom flask, connected to a mechanical stirrer, 200 mL purified hexane was added. To the flask, 1 mL of a 2M solution of tri-ethyl-aluminum (TEAL) in hexane was added. Under stirring conditions subsequently using a Thermal Mass Flow meter (from Brooks) propylene and hydrogen were added at volumetric rates of respectively, 20 L/h and 5 L/h. After saturating the slurry mixture with the gasses, 900 mg of catalyst was dosed as a suspension in hexane. After 5 min, the gas feed was switched to nitrogen, which was passed through the slurry mixture for 3 min followed by stopping the mechanical stirring. After settling of the solid constituents, the top part of the clear solvent was siphoned off and replaced by hexane until a volume of 200 mL was reached. The polymerized catalyst particles were stored as a slurry in hexane. Analysis of the average particle size using SLS showed a D_{50} of ~39 µm and a relative span $\frac{D_{90}-D_{10}}{D_{50}}$ of 0,9.

The catalyst yield, determined to be ~9.2 g iPP per g cat, was calculated indirectly based on Equation (Eq.) S1:

$$D_{50-polymer} = D_{50-catalyst} \cdot R_f \cdot \sqrt[3]{CY+1} \quad \text{[Eq. S1]}$$

Where $D_{50\text{-polymer}}$ is the average particle size of the polymerized catalyst particles and $D_{50\text{-catalyst}}$ that of the pristine catalyst particles, R_f relates to the porosity of the catalyst and polymer particles and the number of polymer particles that originate from a single catalyst particle and is assumed to be 1 here. Finally, CY is defined as the catalyst yield in terms of g PP per g catalyst[9].

SEM images showing the morphology of the propylene polymerized Ziegler Natta catalyst are shown in Figure S3. The particle replica effect is evident with the polymer particle taking over the shape of the pristine catalyst particle, including the still-present cracks from the catalyst drying procedure[10].

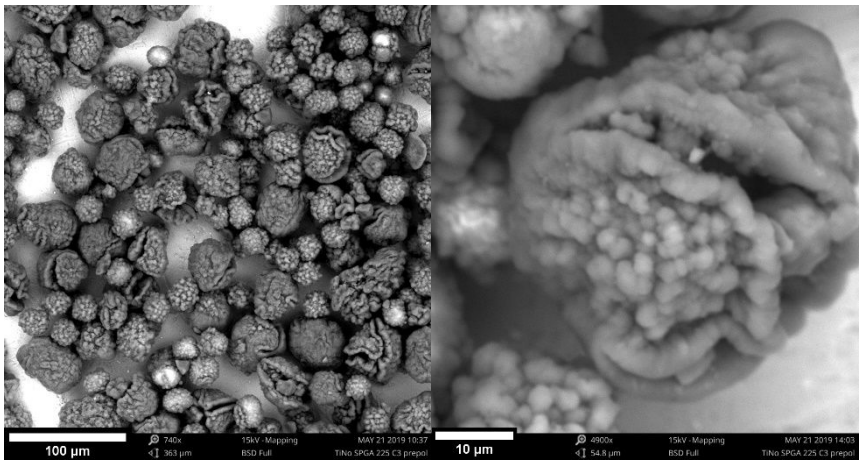

Figure S3 Scanning Electron Microscopy (SEM) images of the propylene polymerized Ziegler-Natta catalyst particles. The morphology of the cracks and the pristine catalyst particles in general is observed to be maintained as isotactic polypropylene is being formed at yields on the order of several g iPP/ g cat. SEM images were taken with a Phenom Pro SEM unit and an accelerating voltage of 15 kV inside a N_2 filled glovebox operating at <1 ppm of H_2O and O_2.

4. Sample Capillary Loading

The polymerized catalyst particles, which were stored in a hexane slurry, were first allowed to settle down after which the majority of the solvent was removed followed by drying the catalyst particles under mild vacuum conditions for 30 min without applying external heat. The polymerized catalyst particles were then loaded into polyimide capillaries purchased from MicroLumen with an outer diameter of 120 µm and walls of 10 µm thick. After loading the capillaries, the ends were dipped into a two-component, low-outgassing and near-hermetic sealing epoxy, code H74, from Epotek. The epoxy was then cured at 80 °C on a hotplate for 30 min. All above mentioned actions were performed in a N_2-filled glovebox operating under 1 ppm of H_2 and O_2. After sealing of the capillaries, they were placed in glass vials sealed with Teflon tape and placed in steel vacuum tubes, sealed off with Viton O-rings suitable for transport.

5. Experimental Details on the X-ray Imaging Setup

The X-ray ptychography and X-ray fluorescence (XRF) datasets were collected with respectively an Eiger X 4M hybrid pixel detector (Dectris Ltd.) and a Maia 384-C X-ray fluorescence detector[11] at the Hard X-ray Micro/Nano-Probe beamline P06 at the PETRA III synchrotron facility, which is part of DESY. Using a golden angle collection approach, subsequent 2-D projections were collected with a constant projection angle increment of 147.5 degrees over multiple full rotations, which increases the number of different projection angles in the range from 0 to 360 degrees with every full rotation. The full range of 360 degrees (instead of just 180, which is sufficient for absorption tomography) was used to check for any possible self-absorption effects in the XRF data. Projection images were collected at 12 keV with a beam size of 160 x 140 nm^2 (h x v) focused using KB mirrors. The polymerized catalyst particle was raster-scanned over an area of 73 x 61 $micron^2$ using a 150 nm step-size. The elemental distribution images were obtained by fitting the obtained single pixel XRF spectra using the GeoPIXE software package[12]. For XRF the 2-D pixel size is equal to the step-size of 150 nm, which was also used for the 3-D voxel size of 150 x 150 x 150 nm^3 after reconstruction. The ptychographic data-sets were reconstructed using in-house developed software. For ptychography the 2-D pixel size obtained was 43.2 nm, which was then used for the 3-D voxel size of 43.2x43.2x43.2 nm^3 after reconstruction.

6. Tomography Reconstruction of the X-ray Ptychography and X-ray Fluorescence Data-sets

For the reconstruction of the collected X-ray Ptychography and XRF tomographs the TXM-Wizard software package was used[13]. Each stack of 2-D projection images of the X-ray Ptychography and XRF datasets were aligned manually to correct for motor jitter and sample movement. The 3-D tomographic slices were reconstructed with an iterative algebraic reconstruction technique (iART). The reconstruction of the above 2-D projections from both the ptychographic and XRF data-sets as well as calculations based on in-house developed MATLAB scripts from subsequent sections were all performed on a consumer laptop with 16 GB of RAM and a 6 core CPU running at 2.20 GHz. Afterwards the Avizo™ software package was used for volume rendering and subsequent analysis of the obtained 3-D tomographic slices. All three data-sets (Cl XRF, Ti XRF, Ptychography) were thresholded and masked to remove low intensity voxels considered to be either intrinsic noise from the raw 2-D projections or artefacts from the 3-D tomographic reconstruction. Then the data-sets were cropped in size to remove any voxels attributed to the reconstructed capillary wall. Table S1 and Figure S4 show respectively the volume, calculated spherical diameter, and histograms of the segmented images of the three data-sets before and after performing thresholding, masking and cropping operations. The correctness of the thresholding and masking was checked by comparing the diameter of virtual particle obtained after thresholding and masking of the ptychographic volume. This diameter was calculated to be 40.6 µm, i.e. very close to the experimentally found D_{50} of the polymerized particles of 39 µm. Furthermore, the calculated diameter of a sphere of the thresholded Ti XRF data volume is 21.9 µm, which is close to the D_{50} of the pristine catalyst of 18 µm, in turn confirming the applied thresholding. The larger calculated diameter for the thresholded Cl XRF volume compared to that of Ti is due to the presence of the Cl-rich bubbles on the particles external surface, which is absent in Ti signal. Based on the following two observations this measured polymerized catalyst particle seems to be representative of the polymerized batch as a whole: 1) The close match of the equivalent spherical diameter of our measured polymer-catalyst composite particle, 40.6 µm, with that of the D_{50} of the bulk polymer batch as measured with static light scattering data, 39 µm, see section 3. 2) The similar morphology of the reconstructed particle with respect to those observed with SEM in figure S3, where the same large cracks are observed throughout multiple polymerized catalyst particles. In future works one could establish a set of metrics as has been shown for the FCC particles with X-ray tomography[14].

Table S1 Volume and diameter* of the segmented X-ray Ptychography, Ti and Cl X-ray Fluorescence data-sets before and after thresholding.

Data-set	Volume (µm³)	Diameter* (µm)
Raw data-set		
X-ray Ptychography	52925	46.6
Cl X-ray Fluorescence	59666	48.5
Ti X-ray Fluorescence	56406	47.6
Thresholded data-set		
X-ray Ptychography	34956	40.6
Cl X-ray Fluorescence	9460	26.2
Ti X-ray Fluorescence	5524	21.9

* The calculated diameter here is that of a sphere with the corresponding volume given in the table.

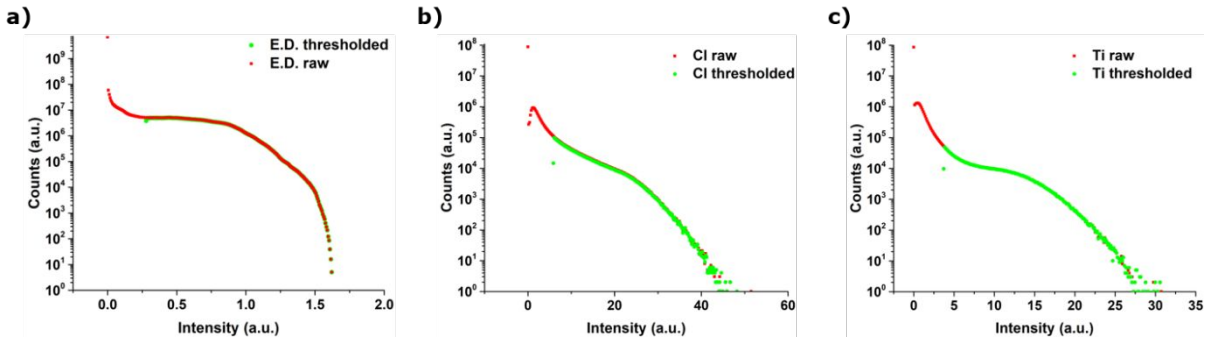

Figure S4 Histograms of (a) electron density obtained from X-ray ptychography, (b) Cl X-ray fluorescence (XRF) intensities and (c) Ti XRF intensities of the raw data-sets in red and the thresholded data-sets in green. With the thresholding, the lowest intensity voxels are filtered out, which are considered to be noise from either the raw 2-D projections or artefacts introduced during the 3D tomographic reconstruction.

Afterwards, the thresholded XRF data-sets were aligned separately with respect to the ptychography data-set in Avizo™ using image registration via an iterative optimization algorithm that computes a transformation for the co-registration of two image data-sets[15].

For the volume rendering and subsequent operations using the Avizo™ software package, a workstation with a Nvidia® Quadro K5000, 128 GB of RAM and two Intel® XEON E5-2687W CPU units with 8 cores running at 3.10 GHz were utilized.

7. Beam-induced Morphology Changes

Following X-ray beam exposure, morphology changes were observed in the catalyst particle during the continuous exposure to the X-ray beam. The effect was mainly visible in the electron density (E.D.) maps and the Cl XRF data-set, whereas the Ti XRF data-set was considerably more stable (i.e. over longer time periods), as evidenced in Figure S5. Due to these beam-induced morphology changes, we chose to use only the first 70 projection images for the 3-D reconstruction, during which very little changes were observed. This lead to an average angular spacing of 4.3 degrees between subsequent projections. The main morphological changes observed in the Cl and E.D. signals are the “bubble”-like regions on the outer surface of the particle which are rich in Cl but absent in Ti signal. As a function of scanning time, these bubbles collapsed and dispersed the Cl within the composite particle. Our hypothesis is that these bubbles originate either from hydration of the $MgCl_2$ framework, which is highly sensitive towards any H_2O impurities, or residual slurry-phase components from an insufficient

drying process. The framework hydration seems less likely due to the careful handling of both the catalyst both before and after polymerization using at all times either Schlenk-line techniques or handling inside a N_2-filled glovebox operating at <1 ppm O_2 and H_2O. Furthermore, the capillaries, which were loaded with the catalyst particles inside an inert atmosphere, were sealed with a low-outgassing and near-hermetic epoxy as discussed in section 4. The second hypothesis suggests that a residual phase of liquid and dissolved components such as ethyl-aluminium-chloride compounds, originating from the reaction of the triethylaluminium co-catalyst with $TiCl_4$, heptane diluent molecules and the donor molecules (a phthalate-based internal donor compound) had not been removed successfully, i.e. completely, from the composite particles during the mild vacuum drying method applied. In this scenario the chlorinated aluminium species would then be the origin of the Cl present in the bubbles and explain the absence of Ti. Unfortunately, Al XRF is not feasible with the instrumental setup used due to the low energy of the Al $K\alpha_1$ emission lines (1.48 keV), which causes strong photon attenuation through air, that is, along the path between polyimide capillary wall and the XRF detector; therefore we could not proof this hypothesis at this stage. However, regardless of whether $MgCl_2$ framework hydration or residual slurry-phase components are the cause of these surface bubbles, we expect that when applying cryogenic cooling conditions to the catalyst particles in future experiments we will drastically minimize beam-induced morphology changes; this approach should therefore become a standard component in the methodology when measuring Ziegler-Natta catalyst particles with intense X-ray sources.

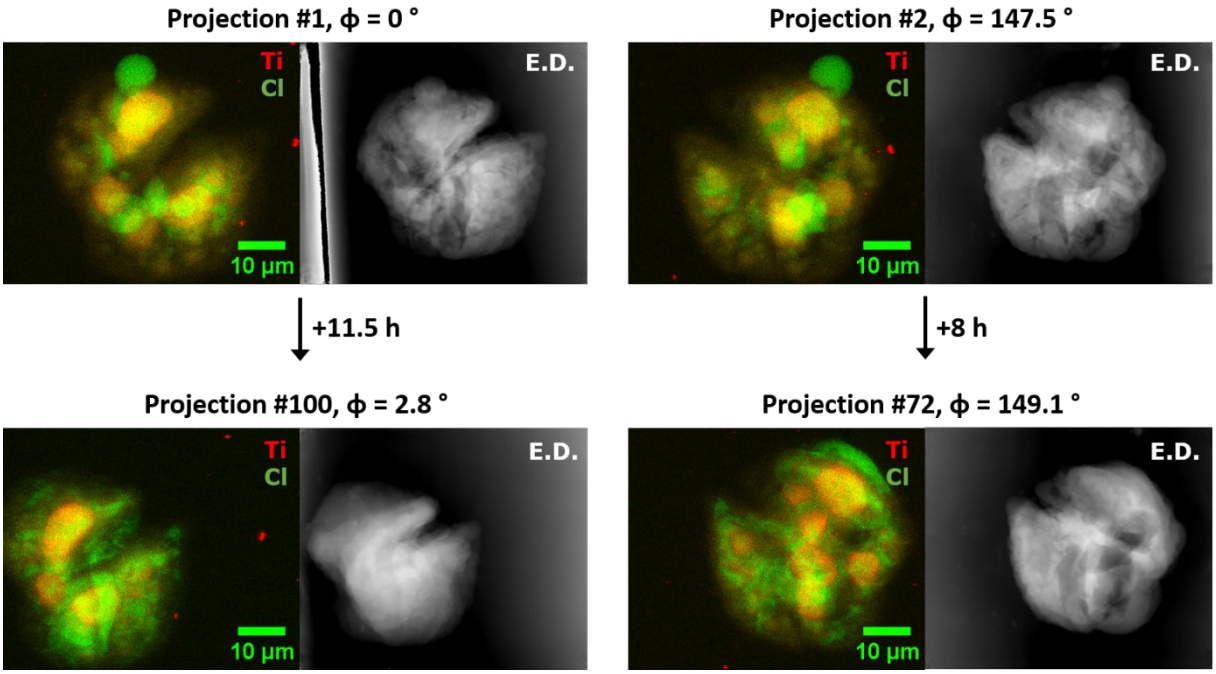

Figure S5 Raw 2-D projections, taken at different angles and time intervals, showing the X-ray beam-induced morphology changes as a function of exposure time. After 8 h of scanning, the Cl XRF signal is observed to be the main contributor to morphology changes, whereas the Ti XRF signal is considerably more stable. At 11.5 h of scanning (projection #100) the overall particle morphology has considerably changed in all three data-sets: the particle appears to have shrunk and the chlorine signal to have been redistributed within the composite particles volume.

8. Estimation of the achieved 3-D Resolution from Reconstructed Data-sets

The 3-D spatial resolution of the ptychography and Ti XRF data-sets was estimated by measuring line profiles on the 2-D generated slices from the reconstructed particle[16,17]. The intensity obtained from the line profiles across the edge of the composite particle (ptychography) or clusters (Ti) were fitted with a Gaussian profile, see equations S2a-c. Here *a* is the height of the fitted peak, *b* is the center position of the peak, and *c* is the standard deviation, related to the full width at half maximum (FWHM). The half width at half maximum value (HWHM) when corrected for the voxel size is taken as an estimate of the resolution at which this edge feature is resolved, as shown in Figures S6,7. Using this approach, for ptychography the 3-D resolution was estimated to be around 400 nm whereas for the Ti XRF data-set it was estimated to be around 600 nm. For the Ti XRF data-set determining the 3-D resolution with the line profile method is more difficult due to the observed layer-by-layer fragmentation of the cluster's surface as discussed in the main text, which therefore would cause broadening of the edge in a line profile. A more routinely used technique to estimate the 3-D resolution is Fourier Shell Correlation (FSC), however this technique requires one to split the original data-set in two data-sets of alternate projections to compare the overlap in Fourier space, which limits its usefulness in this specific case with both a limited number of 2-D projections (35 per data-set when halved) and a slowly changing morphology as a function of beam exposure that introduces extra artefacts when the angular spacing is poor. Nevertheless, in future experiments with a stable particle morphology and a significantly larger number of 2-D projections (preferably upwards of 360) the FSC evaluated resolution should give a more quantitative and reliable estimate of the 3-D resolution obtained throughout the entire particle's volume[18,19]. We expect that the obtained 3-D spatial resolution can further be improved for such studies down to several tens of nm for ptychography and (sub-)100 nm for XRF by optimizing the methodology by using for instance a cryo-cooled stage as is often used in the biological fields when dealing with X-ray sensitive (in-)organic matter[20].

$$f(x) = ae^{-\frac{(x-b)^2}{c^2}} \qquad \text{[Eq. S2a]}$$

$$FHWM\ (voxels) = 2\sqrt{2ln2}\ c \qquad \text{[Eq. S2b]}$$

$$HWHM\ (nm) = \frac{FHWM}{2} \times Voxel\ size \qquad \text{[Eq. S2c]}$$

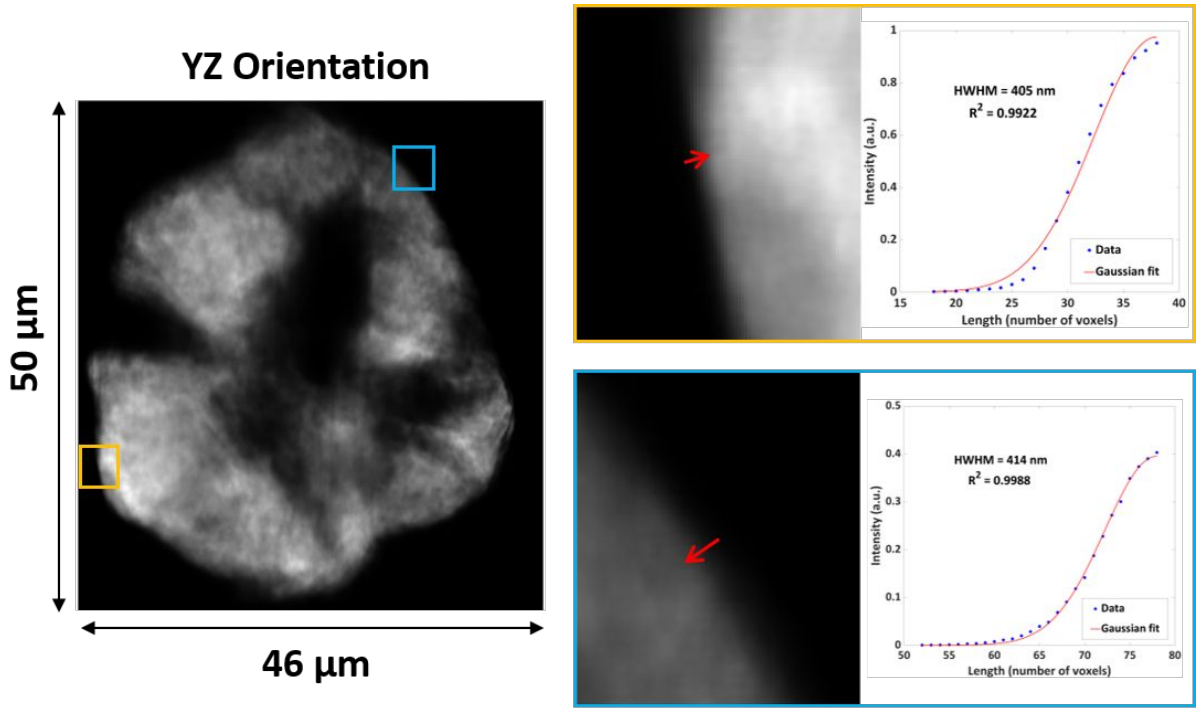

Figure S6 Reconstructed slice in the YZ plane of the ptychography data-set (**Left**). The orange and blue boxes show two edges where a line profile was measured, which gives the intensity as function of the length of the line (**Right**). The half width at half maximum value of the Gaussian fit of these line profiles is taken as an estimate of the achieved resolution at which this edge is resolved.

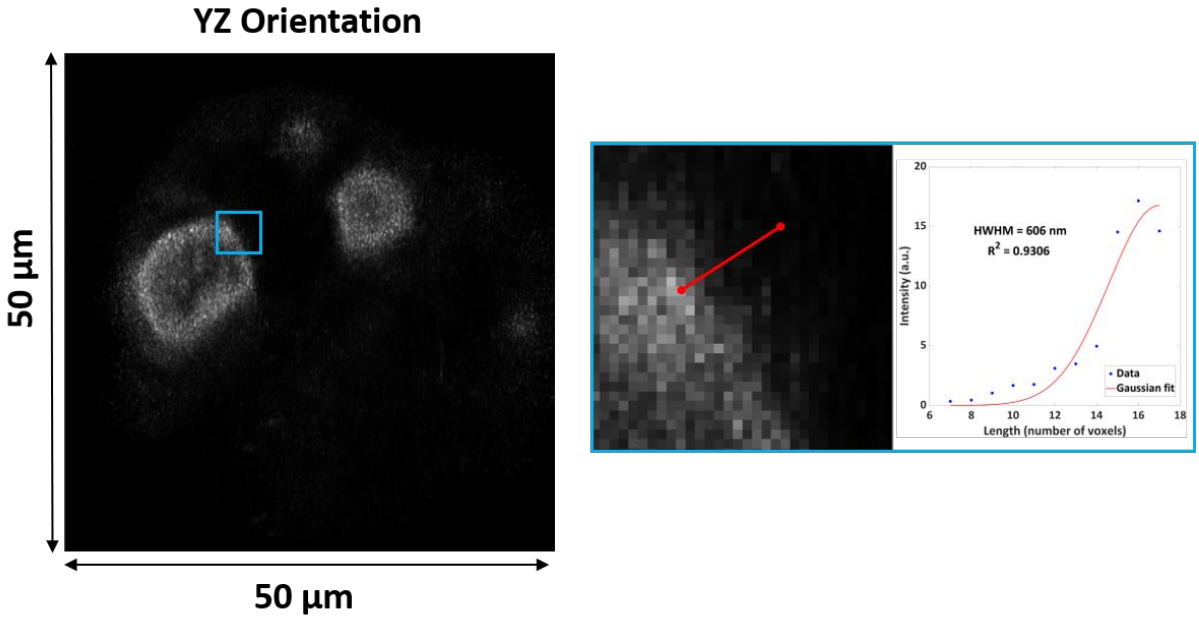

Figure S7 Reconstructed slice in the YZ plane of the Ti XRF data-set (**Left**). The orange and blue boxes show two edges where a line profile was measured, which gives the intensity as function of the length of the line (**Right**). The half width at half maximum value of the Gaussian fit of these line profiles was taken as an estimate of the resolution at which this edge is resolved.

9. Calculated 2-D Projection Images of Reconstructed Datasets

Due to the beam-induced morphology changes it is important to verify that the reconstructed 3-D tomographic slices are a valid representation of the raw 2-D projections. To do this, we have calculated the 2-D projections at the 0 degree angle for each reconstructed data-set by integrating all 3-D tomographic slices, converted into .tiff format images, along the YZ plane. The results are compared in Figure S8. It is evident that the overall particle morphology, for example the presence of the large cracks, is maintained in all three data-sets and therefore validates the reconstruction procedure described earlier. However, in the case of the Cl XRF data-set, the bubble on the particle's external surface, which gradually decayed as a function of scanning time, is not properly reconstructed as is to be expected for a vanishing feature. In the case of the Ti XRF data-set it is clear that the largest clusters are properly reconstructed. The blurriness of the reconstructed 2-D projections as compared to the raw 2-D projections is due to the limited amount of 2-D projections used for the reconstruction, which therefore limits the achieved 3-D resolution of all data-sets.

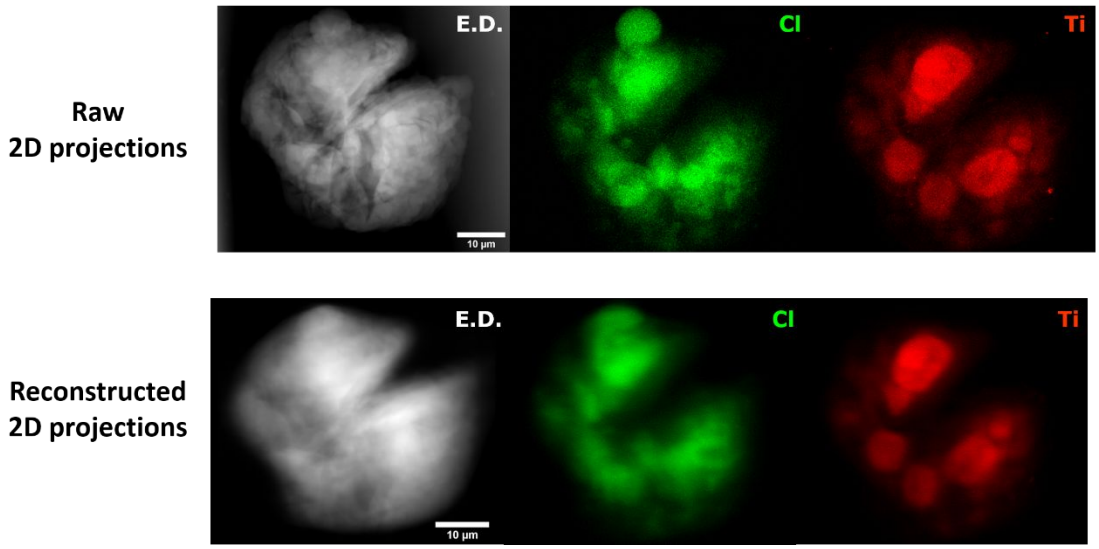

Figure S8 Comparison of the raw (above) and reconstructed (below) 2-D projections at the 0 ° angle of all three data-sets. The comparison of these two data-sets was done to validate the reconstruction parameters (manual alignment, number of projections, algorithm used) chosen for the 3D reconstruction of each data-set.

10. Volume Expansion of Titanium throughout the X-ray Ptychography Dataset

The segmented ptychography data-set, with a voxel size of 43.2 x 43.2 x 43.2 nm^3, was first resampled to the voxel size of the Ti X-ray fluorescence data-set of 150 x 150 x 150 nm^3 voxel size. The center of the polymer-catalyst composite particle was determined based on the segmented ptychography data-set by measuring the Euclidian distance of each voxel from the surface. The voxel(s) with the largest distance was then taken as the center of the entire composite particle's volume. The Ti XRF intensity values were first segmented and then labelled in the Avizo™ software. Here a label is defined as the segmented volume in which a Ti cluster resides, where the Ti cluster is based on the actual grey-scale intensity values. The center of each Ti label was calculated. This was done by measuring the Euclidian distance of each voxel within the label's volume towards the surface of this specific label. The voxel(s) with the largest distance was then taken as the center of this label's volume. Now that the center of the composite particle and that of each Ti label has been calculated the following two parameters were calculated namely; The distance between the center, d_c, and surface, d_s, of each Ti label with respect to the center of the composite particle. In this case we only considered Ti labels, which were larger than 4 voxels in size (5571 labels) due to the achieved Ti XRF 3-D resolution of 600 nm. The distance between the surface of each label and the center of the composite particle, d_s, was calculated by

expanding the volume of the label by one voxel layer until the center of the ptychographic data-set was reached. Then the shortest distance in this expanded layer was used as the distance between the label's surface and the center of the composite particle, d_s. To calculate the distance of the center of each Ti label towards the center of the composite particle, d_c, the shortest path between these two points was used. In Figure S9 the histograms for both the d_c and d_s values are given. The high average distance of all Ti labels from the center of the particle, ~18.7 micron, which is close to the radius of the composite particle of 20.3 micron shows that the Ti active sites are being pushed away from the center of the expanding composite particle's center due to the growth of the polymer. The large number, 5443, of Ti labels smaller than 0.135 μm^3 or 40 voxels in size shows that the layer-by-layer fragmentation model is also occurring alongside the continuous bisection fragmentation model within the composite particle as these small fragments must originate and therefore have been peeled off the surfaces from the six largest Ti labels.

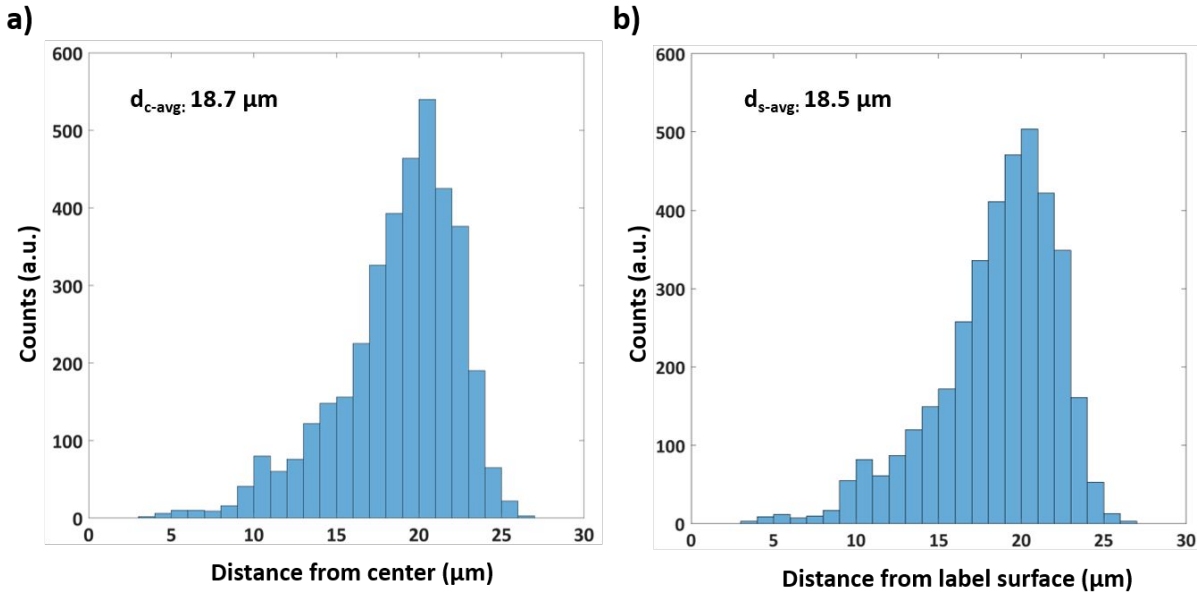

Figure S9 Histograms showing the frequency of the distance between the centre of the segmented Ti clusters, d_c, and that of the composite particle (a) and the frequency of the distance between the surface of the segmented Ti clusters, d_s, and that of the composite particle with a voxel size threshold 4, corresponding roughly to the estimated 3-D resolution of the Ti XRF data-set.

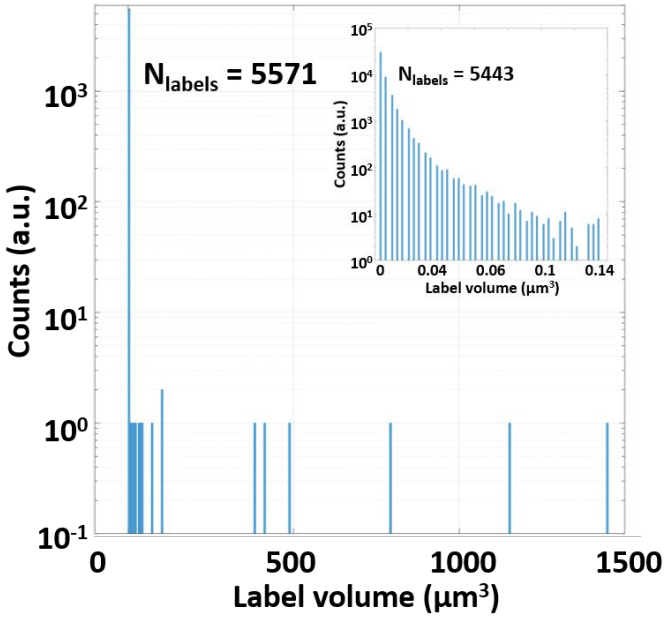

Figure S10 Histogram showing the frequency of the volume of all Ti labels larger than 4 voxels in size. From the 5571 Ti labels, 5443 Ti labels are smaller than 0.135 µm^3, which corresponds to 40 voxels in size.

11. Radial Distribution of Titanium Within Clusters

The radial distribution of Ti throughout the volume of each label as defined in section 10 was calculated. For the six largest labels as shown in Figure 3A, which represent the six largest Ti clusters as shown in Figure 2B, distance maps were calculated for the 3-D volumes within each individual label providing the distance of each voxel in the label from its surface. The respective volumes of the total segmented and labelled data-sets are given in Table S2, with the sixth largest labels corresponding to 85% of the total segmented volume and the subsequent largest label only representing 1.8% of the total volume (compared to 6.9% for the sixth largest label). The mean Ti intensity of each label was then calculated as a function of distance from the surface of each label towards the center voxel of the label. The morphology and cross-sections of the Ti clusters present within the six largest labels are shown in Figure S11. For the red and blue labels, it is clear that these labels don't consist of one single Ti cluster as is observed for the other four labels, but instead is build-up from respectively four individual sub-clusters inside the red label volume or two individual sub-clusters inside the blue label volume. Based on the shape of the sub-clusters inside the blue and red labels it seems that these sub-clusters are the result of a cleaved, single large cluster due to stress induced inside the porous structure of the support framework by the growing polymer chains. A virtual cut through the two individual sub-clusters within the blue label reveals a similar trend as observed for the other clusters with an enrichment of Ti at the edge and a depletion of Ti in the core. At higher polymerization yields, these two individual sub-clusters, as well as the other clusters, would therefore likely fragment into smaller units by breaking up through the cluster's center until finally the primary particle size of a few tens of nm is reached for $MgCl_2$. The heterogeneity in the fragmentation rate between the different Ti clusters is likely due to a non-uniform distribution of cracks and macroporosity within the pristine catalyst particle. Another explanation would be that of local heat and mass transfer limitations, however these are not expected to play a significant role here due to the mild reaction conditions as has been shown experimentally by Noristi *et al.,* for a series of propylene polymerized Ziegler-Natta catalysts at different polymer yields[21].

Table S2 Volume and box dimensions of the entire Ti segmented volume and the sixth largest labels.

Data-set	Volume (µm³)	Bounding box dimensions X,Y,Z (µm)
Total Ti segmented volume	5524	54,60,60
Pink label	1449	19,19,19
Green label	1155	19,19,19
Blue label	794	19,19,19
Orange label	486	12,14,15
Cyan label	411	15,13,15
Red label	380	19,19,19

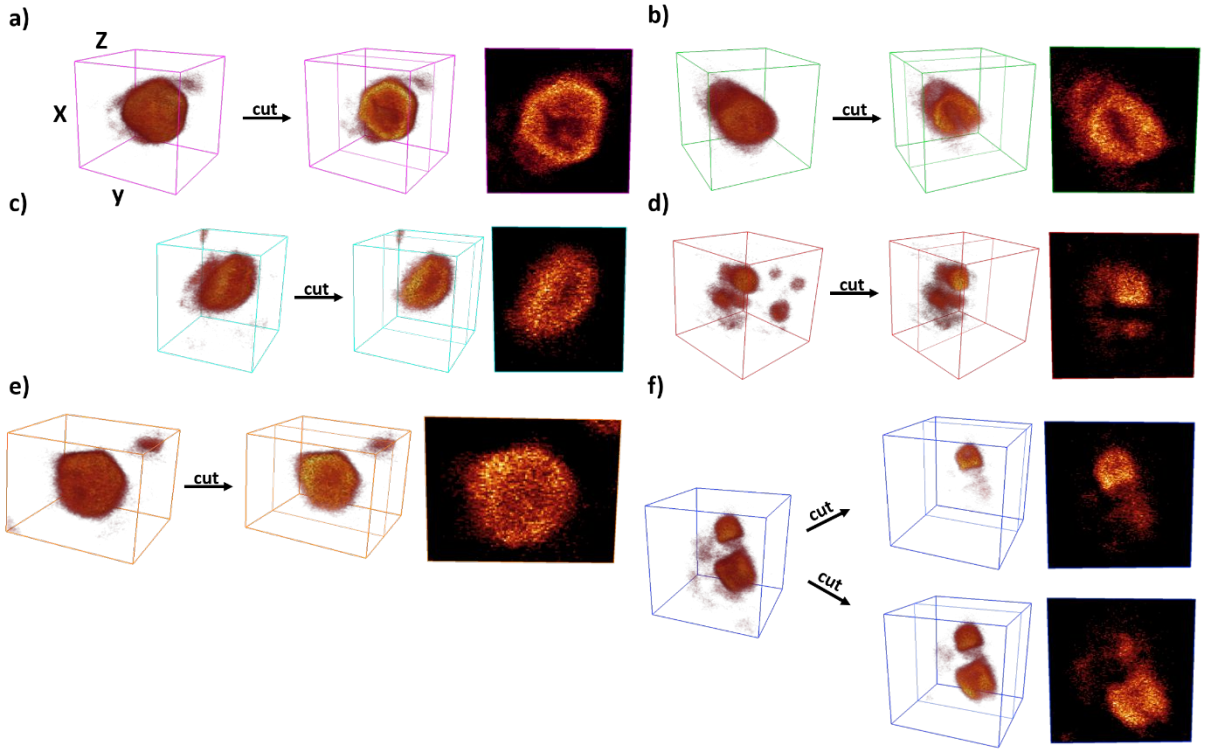

Figure S11 Zoom-in of the titanium clusters with and without a clipping plane shown in 3-D and the corresponding 2-D slice belonging to the six following labels from Figure 3. (a) the pink label (b) the green label (c) the cyan label (d) the red label (e) the orange label (f) the blue label with two cuts corresponding to the two sub-clusters or fragments. The dimensions of each bounding box and volume of the corresponding labels are given in Table S2.

12. Possible Self-absorption Effects in X-ray Fluorescence Tomography

The lower intensity of Ti at the core of each cluster with respect to the edge of the cluster could also be due to self-absorption effects. Self-absorption occurs if significant absorption of X-rays along the pathway out of the sample takes place[22,23]. This can be the case if the pathway becomes very long for large samples or if the material through which the emitted X-ray photons have to pass is strongly absorbing at the energy of the X-ray emission line. This absorption is a function of energy, atomic number, and density and the effect is called self-absorption because the fluorescence of a part of the sample is absorbed by other parts of the sample itself. In this case for example the Ti K fluorescence (4.51 and 4.93 keV) emitted at the center of a large (spherical) particle will be absorbed by Ti (and other elements with an absorption edge above 4.93 keV) present e.g. in the surface (or homogenously everywhere) in the particle. If self-absorption becomes significant, this will erroneously result in the measurement of a shell-like distribution of Ti, because Ti K X-ray emission from the core is more strongly re-absorbed by the Ti species in the particle than emission from near surface regions and therefore would make it seem like the core has a lower Ti intensity with respect to the edge[22]. To proof that this is not an issue in the present case to any significant extent, in Figure S12 the region used for the pink label is compared for both the Ti XRF and Cl XRF data. Since the fluorescent X-rays from the K shell of Cl are emitted at a much lower energy of ~2.6 keV with respect to Ti at ~4.5 keV, any self-absorption effect should be considerably larger for Cl due to the shorter penetration depth for a photon of lower energy through the same material volume. As observed based on both visualization and the line-profile the intensity of Cl is more or less constant from the edge of the cluster to the core (and even higher on average than that of Ti as expected due to the lower wt% of Ti in the catalyst with respect to Cl, which corresponds to roughly 75 wt% in pure $MgCl_2$), whereas the Ti intensity drops significantly in the core as compared to the edge. This therefore means that self-absorption effects can be ruled out as the reason for the drop of Ti intensity in the core as the same behavior should then have been observed (and even stronger) for Cl.

However, this observation is also interesting from a different perspective: the more or less constant intensity of Cl in the core of the cluster with respect to the edge would disagree with the statements made earlier that the Ti clusters are fragmenting through the core as is expected in the continuous bisection fragmentation model. This is because the same trend for the Cl intensity would then be expected. However, as mentioned in appendix section 3, the bubbles observed to be rich in Cl and poor in Ti on the external particle's surface are likely residual slurry-phase components like the chlorinated Al co-catalyst, heptane diluent and silane external donor molecules. These same components are then also expected to be present within these Ti rich clusters close to the active sites and where the polymer is being formed. Thus our observation does not imply that the core of these clusters was rich in $MgCl_2$ framework species but instead of residual slurry-phase components.

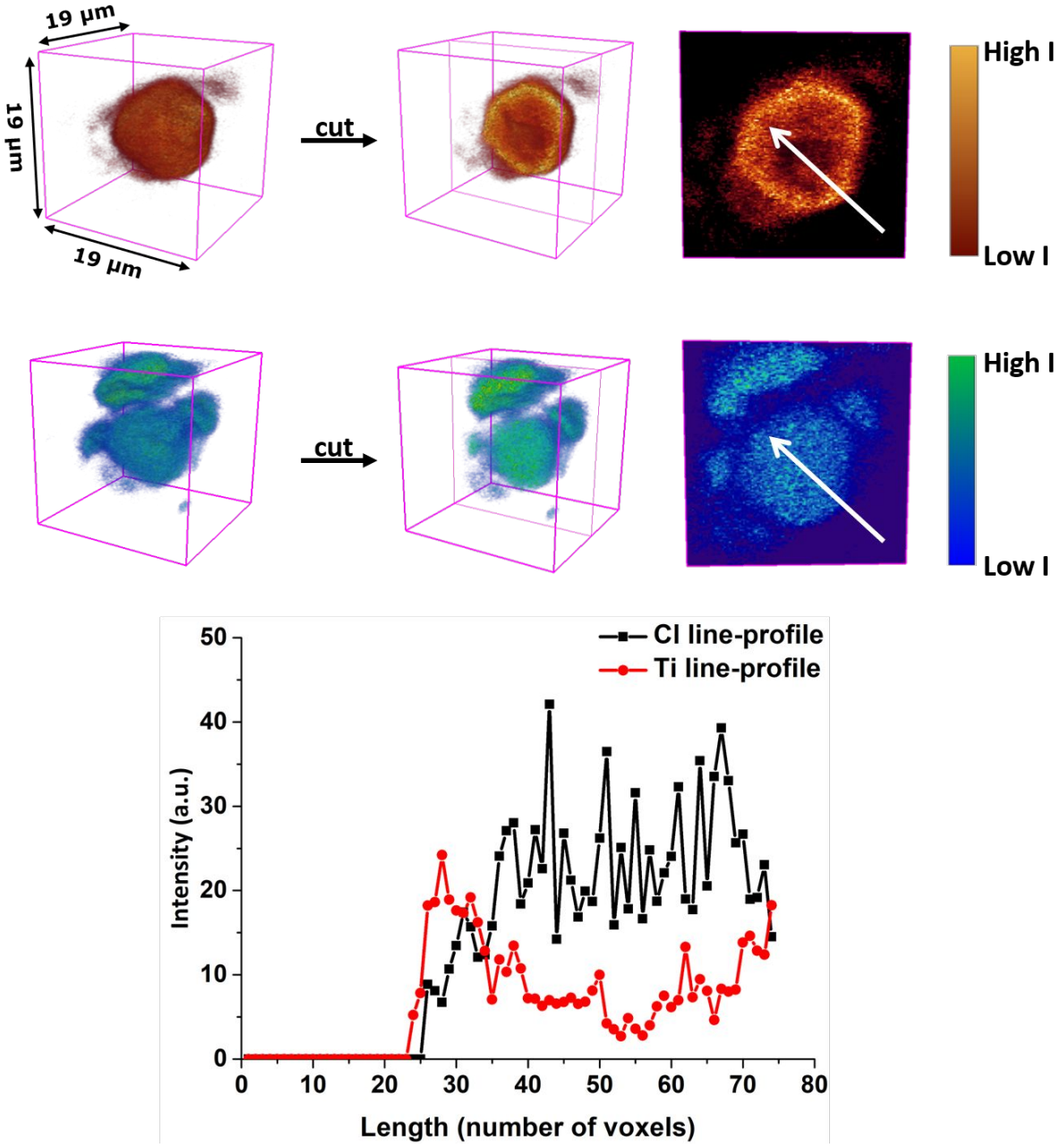

Figure S12 Comparison of the intensities of Ti XRF and Cl XRF in the interior of the same cluster. A line profile was obtained at the same positions and compared. It clearly shows that the Cl intensity is more or less constant throughout the centre of the cluster whereas the Ti intensity is significantly higher at the two edges than the centre of the cluster.

13. References

[1] Laurence, R.L. and Chiovetta, M.G., In: Reicher, K.H., Geisler, G. (Eds.), Polymer Reaction Engineering, Hasuer-Verlag, München, **1983**, 74-112.

[2] Weickert, G., Meier, G.B., Pater, J.T.M., Westerterp, K.R., The particle as microreactor: Catalytic propylene polymerizations with supported metallocenes and Ziegler-Natta catalysts, *Chem. Eng. Sci.*, **1999**, 54, 3291-3296.

[3] Fink, G., Steinmetz, B., Zechlin, J., Przybyla, C., Tesche, B., Propylene polymerization with silica-supported metallocene/MAO catalysts, *Chem. Rev.,* **2000**, 100, 1377-1390.

[4] Pater, J.T.M., Weickert, G., Loos, J., van Swaaij, W.P.M., High precision prepolymerization of propylene at extremely low reaction rates—kinetics and morphology, *Chem. Eng. Sci.,* **2001**, 56, 4107-4120

[5] Abboud, M., Denifl, P., Reichert, K.H., Fragmentation of Ziegler-Natta Catalyst Particles During Propylene Polymerization, Macromol. Mater. Eng., **2005**, 290, 558-564.

[6] Zheng, X., Loos, J., Morphology evolution in the early stages of olefin polymerization, *Macromol. Symp.,* **2006**, 236, 249-258.

[7] Horácková, B., Grof, Z., Kosek, J., Dynamics of fragmentation of catalyst carries in catalytic polymerization of olefins, Chem. Eng. Sci., **2007**, 62, 5264-5270.

[8] Ramjoie, Y.J.E., Vlaar, M., Friederichs, N.H., Sergeev, S.A., Zakharov, V.A., Bukatov, G.D., Taftaf, M., Aburaqabah, A., *European Patent 2027164*, **2007**

[9] Lafleur, S., Berthoud, R., Ensinck, R., Cordier, A., De Cremer, G., Philippaerts, A., Bastiaansen, K., Margossian, T., Severn, J.R., Tailored bimodal ultra-high molecular weight polyethylene particles, *J. Polym. Sci. A.,* **2018**, 56, 1645-1656

[10] McKenna, T.F.L., Di Martino, A., Weickert, G., Soares, J.B.P., Particle Growth During the Polymerisation of Olefins on Supported Catalysts, 1 – Nascent Polymer Structures, *Macromol. React. Eng.*, **2010**, 4, 40-64

[11] Ryan, C.G., Siddons, D.P., Kirkham, R., Dunn, P.A., Kuczewski, A., Moorhead, G., De Geronimo, G., Paterson, D.J., de Jonge, M.D., Hough, R.M., Lintern, M.J., Howard, D.L., Kappen, P., Cleverley, J., The New Maia Detector System: Methods For High Definition Trace Element Imaging Of Natural Material, *AIP Conf. Proc.*, **2010**, 1221, 9-17

[12] Ryan, C.G., Laird, J.S., Fisher, L.A., Kirkham, R., Moorhead, G.F., Improved Dynamic Analysis method for quantitative PIXE and SXRF element imaging of complex materials, *Nucl. Instrum. Methods Phys. Res. B*, **2015**, 363, 42-47

[13] Lui, Y., Meirer, F., Williams, P.A., Wang, J., Andrews, J.C., Pianetta, P., TXM-Wizard : a program for advanced data collection and evaluation in full-field transmission X-ray microscopy, *J. Synchrotron Radiat.,* **2012**, 19, 281-287

[14] Meirer, F., Kalirai, S., Morris, D., Soparawalla, S., Yijin, L., Mesu, G., Andrews, J.C., Weckhuysen, B.M., Life and death of a single catalytic cracking particle, *Sci. Adv.,* **2015**, 1, e1400199

[15] Studholme, C., Hill, D.L.G., Hawkes, D.J., An overlap invariant entropy measure of 3D medical image alignment, *Pattern Recognit.,* **1999**, 32, 71-86

[16] Holler, M., Diaz, A., Guizar-Sicairos, M., Karvinen, P., Färm, E., Härkönen, E., Ritala, M., Menzel, A., Raabe, J., Bunk, O., X-ray ptychographic computed tomography at 16 nm isotropic 3D resolution, *Sci., Rep.,* **2004,** 4, 3857

[17] Wise, A.M., Weker, J.N., Kalirai, S., Farmand, M., Shapiro, D.A., Meirer, F., Weckhuysen, B.M., Nanoscale Chemical Imaging of an Individual Catalyst Particle with Soft X-ray Ptychography, *ACS Catal.,* **2016**, 6, 2178-2181

[18] van Heel, M., Schatz, M., Fourier shell correlation threshold criteria, *J. Struct. Biol.,* **2005**, 151, 250-262

[19] Nieuwenhuizen, R.P.J., Lidke, K.A., Bates, M., Puig, D.L., Grünwald, D., Stallinga, S., Rieger, B., Measuring image resolution in optical nanoscopy, *Nat. Methods,* **2013**, 10, 557-562

[20] Carzaniga, R., Domart, M.-C., Collinson, L.M., Duke, E., Cryo-soft X-ray tomography: a journey into the world of the native-state cell, Proto-plasma, 2014, 251, 449-458
[21] Noristi, L., Marchetti, E., Baruzzi, G., Sgarzi, P., Investigation on the particle growth mechanism in propylene polymerization with MgCl2-supported ziegler–natta catalysts, *J. Polym. Sci.*, **1994**, 32, 3047-3059
[22] Kalirai, S., Boesenberg, U., Falkenberg, G., Meirer, F., Weckhuysen, B.M., X-ray Fluorescence Tomography of Aged Fluid-Catalytic-Cracking Catalyst Particles Reveals Insight into Metal Deposition Processes, *ChemCatChem,* **2015**, 7, 3674-3682
[23] Liu, Y., Meirer, F., Krest, C.M., Webb, S., Weckhuysen, B.M., Relating structure and composition with accessibility of a single catalyst particle using correlative 3-dimensional micro-spectroscopy, *Nat. Comm.,* **2016**, 7, 12634